

LOCAL COHESION OF SPLATS IN HYBRID PLASMA SPRAY COATING AS OBSERVED BY IN-SITU EXPERIMENT

RADEK MUŠÁLEK^{a,*}, TOMÁŠ TESAŘ^a, JAKUB MINAŘÍK^{a,b}, JONÁŠ DUDÍK^{a,c}

^a Czech Academy of Sciences, Institute of Plasma Physics, U Slovanky 2525/1a, 182 00 Prague, Czech Republic

^b Czech Technical University in Prague, Faculty of Mechanical Engineering, Karlovo náměstí 13, 121 35 Prague, Czech Republic

^c Czech Technical University in Prague, Faculty of Nuclear Sciences and Physical Engineering, Trojanova 13, 120 00 Prague, Czech Republic

* corresponding author: musalek@ipp.cas.cz

ABSTRACT. Hybrid plasma spraying combines spraying of dry coarse powders and liquids (suspensions and/or solutions). Introduction of secondary miniature phase from the liquid may provide new coating functionality but also may have a significant influence on the local coating cohesion – increasing or decreasing it, depending on the materials combination and deposition conditions. In this study, cohesion of dissimilar splats within the early-stage experimental hybrid thermal barrier coating (TBC) was evaluated by in-situ SEM three-point bending (3PB) observation coupled with high-resolution strain mapping. Loading was carried out on the annealed sample simulating in-service thermal exposure. Observed coating failure confirmed that the coating exhibits a rather high intersplat cohesion lowering its strain-tolerance, which was presumably the reason for the relatively low thermal cycling resistance of the deposit.

KEYWORDS: Plasma spraying, hybrid coating, in-situ SEM, strain mapping, cohesion.

1. INTRODUCTION

Plasma spraying is a versatile method used for the preparation of various protective coatings [1]. Conventional deposition from coarse powders provides high deposition rate and lamellar microstructure, whereas deposition from liquids (suspensions or solutions) provides a new class of coatings microstructures with miniature splats [2]. A cross-over of these two techniques is so called hybrid plasma spraying (Figure 1-left), where powders and liquids are injected simultaneously into the plasma jet with an intent to combine benefits of both types of feedstocks [3, 4]. Generally, powder-originated splats serve here as a matrix, whereas the miniature (secondary) splats are intended to provide an additional coating functionality.

Hybrid spraying is currently used namely for the development of tribological coatings for wear-intensive applications [5, 6]. In our laboratory, the first experimental hybrid thermal barrier coatings (TBCs) were recently deposited by hybrid water-/argon stabilized plasma torch (WSP-H). Yttria-stabilized zirconia (YSZ) was used as the matrix and YSZ, Al₂O₃, gadolinium zirconate (GZO) and yttrium aluminum garnet (YAG) as the secondary phase [7]. Deposited coatings showed promising thermal insulation properties and phase stability but their thermal cycling fatigue lifetimes were inferior to the reference conventional coatings, presumably due to their insufficient strain tolerance caused by a rather dense microstructure.

Straining of hybrid YSZ-YSZ and YSZ-Al₂O₃ coatings was already studied in [8] by in-situ experiment supplemented with strain mapping [8]. General task of strain mapping is to find spatial transformation of the source micrograph into the new “deformed” micrograph (Figure 1-right). From the field of displacement vectors, field of strains can be evaluated and transformed into so called strain maps. Localized straining in strain maps highlights changes in the material microstructure which are often hardly visible to the naked eye. In the case of relatively brittle thermally sprayed coatings, excessive localized straining usually means activation of coating failure, typically by cracking of splats, their mutual sliding, propagation of magistrate cracks or debonding of the coating from the substrate.

Strain mapping algorithms usually work with sub-pixel precision but demand significant computational power especially if sequences of high-resolution strain maps are desirable. Older custom-made strain mapping procedure used in our laboratory was based on adapted MATLAB code using cross correlation method [9]. Recently, a new open-source pixel-wise GCPU_OpticalFlow software using fast pyramidal approach developed by Chabib et al. [10] was adapted in our laboratory.

Aim of this study was to carry out an additional experiment for YSZ-Al₂O₃ sample after the heat-treatment simulating short exposure to jet-engine relevant temperature and, in particular, to test and validate the updated strain-mapping algorithms enabling the tracking of the coating failure evolution at

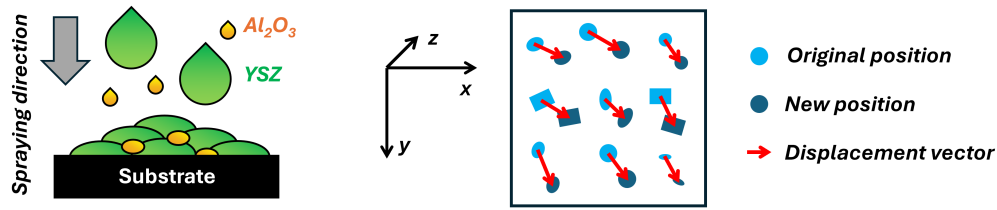


FIGURE 1. Left) Scheme of hybrid spraying combining deposition of YSZ from powder and miniature Al_2O_3 from suspension. Right) Principle of displacement vectors evaluation for strain mapping.

higher spatial and temporal resolution. Relating the microstructural changes incrementally to the preceding loading stage (instead of to the initial unloaded stage) also helps to relate the failure areas to the local coating microstructure as it travels during the experiment within the observed field of view.

2. MATERIALS AND METHODS

The coating sample was prepared by hybrid water/argon-stabilized plasma torch WSP-H 500 (ProjectSoft HK, a.s., Czechia) using Hastelloy-X coupon, NiCrAlY bond-coat and hybrid YSZ- Al_2O_3 top-coat. Amperit NiCrAlY 413.006, YSZ 831.006 (both Höganäs, Germany) powders, and water-based Al_2O_3 suspension (Treibacher Industrie AG, Austria) with 40 wt.% solid load and mean particle size $1.5 \mu\text{m}$ were used as feedstocks for the deposition. More detailed information on sample preparation is provided in [7].

In order to simulate thermal exposure of the coating without introducing large-scale coating failure, sample was annealed for 5 hours at 1150°C in air ($10^\circ\text{C min}^{-1}$ heating ramp, 5°C min^{-1} cooling ramp).

Heat treated sample was cut into form of “match-stick” type specimens with length ~ 28 mm. The side of the sample showing coating cross-section was polished up to colloidal silica polishing step (using OP-S suspension, Struers, Denmark) providing planar scratch-free surface for observation. The final cross-section of the sample was 1.70×1.66 mm (width \times height). Thickness of the substrate, bond-coat, and top-coat were 1.24 mm, 0.13 mm, and 0.29 mm, respectively.

Sample was then inserted into in-situ loading stage Microtest 200 N (Deben, UK) which was mounted in the EVO MA15 (Carl Zeiss, Germany) SEM microscope. Loading was carried out using 3-point bending setup with outer support span $L = 23$ mm. Diameter of the loading pins was 4 mm. After each $50 \mu\text{m}$ of deflection, loading was paused, sample position in the field of view was re-aligned, and SEM image was acquired with high resolution (2048×1536 pixels). Back-scattered electron imaging mode was used in order to visualize spatial distribution of phases with different mean atomic number. Heterogeneous microstructure pattern of the coatings could be directly used for the evaluation of local displacement fields using fast GCPU_OpticalFlow software [10]. From

the displacement fields, strain-maps were evaluated for every pixel of the SEM images in terms of in-plane ε_{xx} (parallel to the coating-substrate interface), out-of-plane ε_{zz} (spraying direction perpendicular to the coating-substrate interface), and engineering shear strain ε_{xy} components.

Equivalent strain field was computed from the strain field components according to the formula [11]:

$$\varepsilon_{eq} = \sqrt{\varepsilon_{xx}^2 + \varepsilon_{yy}^2 + 2\varepsilon_{xy}^2}. \quad (1)$$

Unlike in our previous study [8], strain maps were not related to the initial stage (pristine microstructure before loading), but to the preceding loading step. This approach also allowed to overcome difficulties with the strain evaluation in the areas close to the image edges, which gradually travelled out of the field of view, producing undesirable imaging artifacts.

3. RESULTS AND DISCUSSION

Microstructure of the as-prepared coating in the area above the central loading pin is shown in Figure 2. As intended, the coating consisted of hybrid YSZ- Al_2O_3 top-coat, on top of metallic NiCrAlY bond-coat, on top of Hastelloy-X substrate. The heat exposure induced distinguishable bond-coat oxidation. Within the top-coat, miniature Al_2O_3 splats were well distinguishable among larger splats of YSZ matrix. Some intermingling of both phases was observed, preferentially on top of the miniature phase. Such asymmetric interaction is given by the different capabilities of both coarse and fine splats to remelt underlying material [12]. However, onset of interaction around the whole circumference of Al_2O_3 splats was observed due to the heat exposure. Moreover, pores and intersplat cracks may be discerned from the micrographs. Some vertical pre-cracks were also observed within the coating microstructure, presumably due to the rather low spraying (“stand-off”) distance resulting in high sample temperature during the deposition. This led to a significant densification of the coating and partial development of the vertical cracks. These are not necessarily detrimental as such opening cracks are intentionally induced in so-called vertically cracked thermal barrier coatings (DVC-TBC) to improve the strain tolerance of the coatings [13]. This strategy is

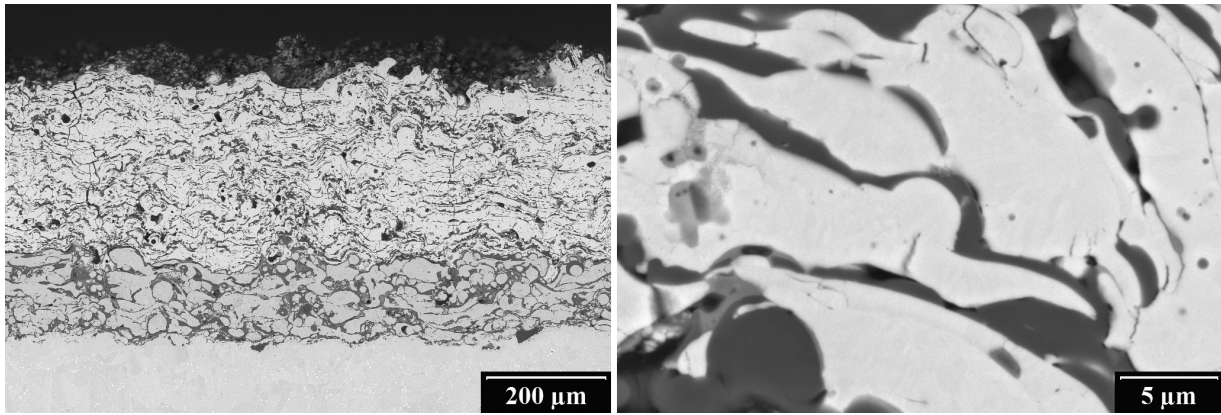


FIGURE 2. Cross-section of the samples. Left) Overview. Right) detail of the top-coat, bright phase YSZ, dark phase Al_2O_3 . Intermediate phase visible on top of some Al_2O_3 splats (semi-grey phase).

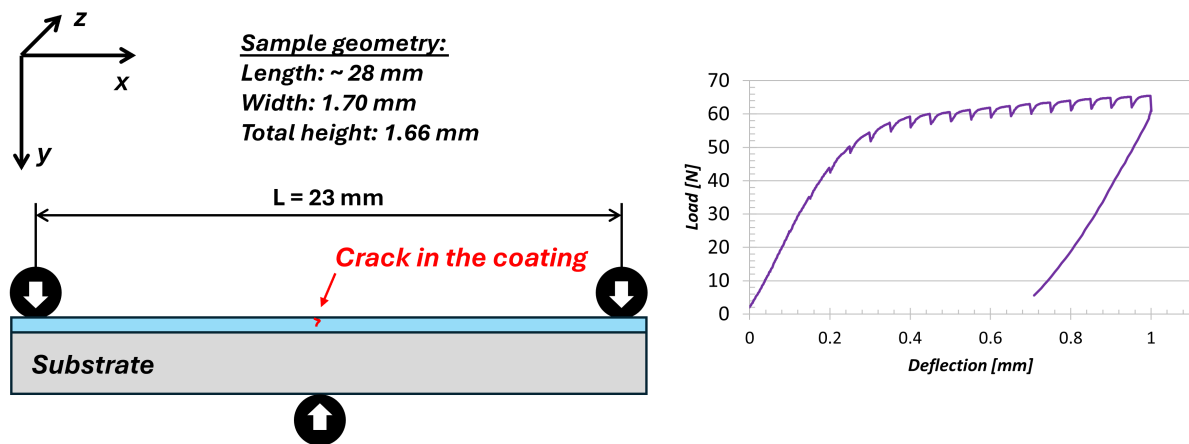


FIGURE 3. Left) Scheme of in-situ 3-point bending experiment. Right) Load curve obtained during in-situ 3-point bending experiment.

an alternative to production of conventional porous TBCs with loose microstructure.

The experimental setup and loading-deflection curve obtained during the in-situ experiment are shown in Figure 3. The loading was elastic up to approx. 40 N after which the plastic loading of the substrate took over. During the SEM image acquisition, the load partially dropped showing characteristic periodic steps on the loading record. Stiffness of the substrate compared to the coating is too big to see cracking of the coating from the plot. From the sample thickness h (given by the sum of thickness of the substrate and individual sub-layers), support span L , and sample deflection D , macroscopic theoretical flexural strain $\varepsilon_{theoretical}$ was evaluated individually for substrate, bond-coat and top-coat surfaces without considering any coating failure according to the classic formula for 3-point bending:

$$\varepsilon_{theoretical} = \frac{6Dh}{L^2}. \quad (2)$$

It should be noted that as first approximation, it was assumed that the neutral plane of the sample passed through the middle of the sample thickness. The over-

all straining of the top-coat was significantly higher (1.88 %) when compared to the substrate-coating interface (1.40 %). At such strains, the coating was obviously already damaged, as observed at the end of the test (Figure 4). However, as the stiffness of the substrate was far greater than the stiffness of the coating, evolution of the coating failure did not have any visible influence on the loading curve. Loading curves must therefore be coupled with the SEM observation or better with the strain mapping, showing directly the coating failure from its very beginning.

Figure 4 illustrates the final appearance of the sample after the test, showing clearly set of several major through-thickness cracks with the mean spacing of 360 μm in the central area stretching from the coating surface towards the substrate. All cracks propagated fairly vertically with minimum in-plane branching. Occasionally, the internal fracture surfaces could be observed directly within the open cracks (Figure 5). It is notable to mention that the fracture propagated in the out-of-plane direction without significant interaction with the secondary phase both in the polished plane, and deeper in the bulk of the coating as observed on the fracture surfaces. The observation on the polished cross section may be thus considered

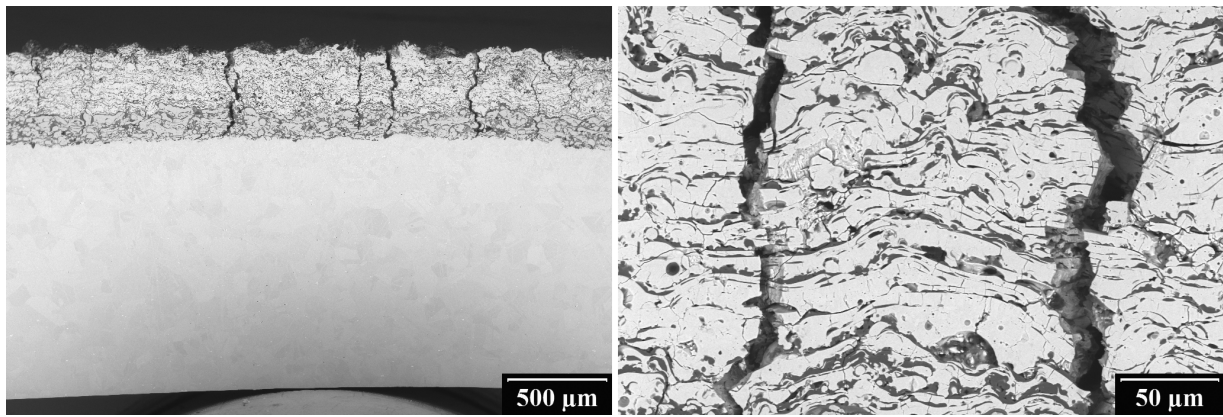


FIGURE 4. Left) Overview of the sample after the test. Central loading pin is visible at the bottom of the image. Right) Detail of crack within the top-coat above the central pin.

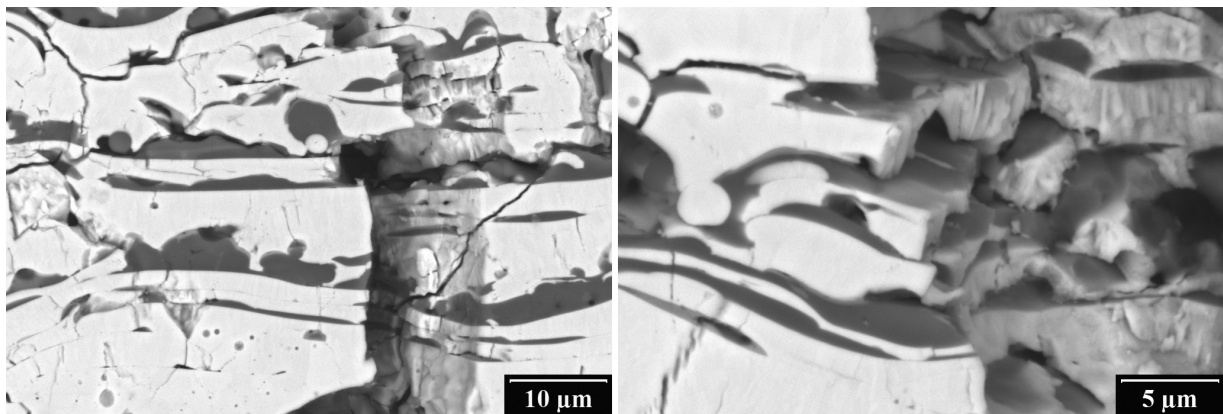


FIGURE 5. Detail of cracks from Figure 4 propagating through the top-coat.

representative for the whole coating. Moreover, the fraction of the secondary phase on the fracture surface corresponded to the overall content of the miniature phase on the coating cross-section. This means that the secondary phase splats were not the weakest spots in the coating structure promoting the crack propagation, because should the opposite be true, the content of the secondary phase splats (or even their clusters) on the internal fracture surfaces would be significantly higher than its overall content in the coating microstructure.

The selection of images declaring gradual propagation of the cracks above the central loading pin during the in-situ experiment is illustrated in Figure 6. For each image of the sequence, strain of each sub-layer was evaluated from the changing distance of two characteristic features preselected on top of substrate and each sub-layer. The original distance of each pair of reference points was approximately 0.9 mm, i.e., $\sim 90\%$ of width of view of the images used for the evaluation (see Figure 6). With increasing loading, the distance between the reference points increased due to the straining of the material and evolution of multiple cracks between them. It is obvious that the level of local strain evaluated by such image analysis (IA) was significantly higher than the macroscopic theoretical strain evaluated from the deflection, also better re-

flecting the ongoing coating failure by changes of the slope of the curves (see Figure 7). As expected, straining of the top-coat was the highest due to its greater distance from the specimen neutral axis. Nevertheless, such manual strain analysis is not only tedious, but provides only general information about the straining of the layers along one dimension.

Finally, from the sequence of micrographs, the detailed area of propagation of two major cracks (see Figure 4-right) was selected for the 2D computer aided strain mapping (Figure 8). Displacement and strain fields were evaluated for each pixel of the regions of interest (788×1051 pixel). Strains were related to the preceding loading step using default settings of the GCPU_OpticalFlow code with *size_median_filter* = 5 and *lambda parameter* = 5.0×10^5 . Although the option of GPU-accelerated computing with CUDA Toolkit libraries was not available on the used workstation (MS Windows 11 Pro, Intel i5-13500 processor, 32 GB RAM), processing of each step took only 27.4 ± 3.2 seconds, so the whole batch of 20 high resolution images was processed in less than 10 minutes. For comparison, processing of just one loading step using our previous strain mapping code based on MATLAB cross-correlation routine [9] took 37 minutes, which is ~ 80 times longer. Another benefit of pyramidal approach is that it does not re-

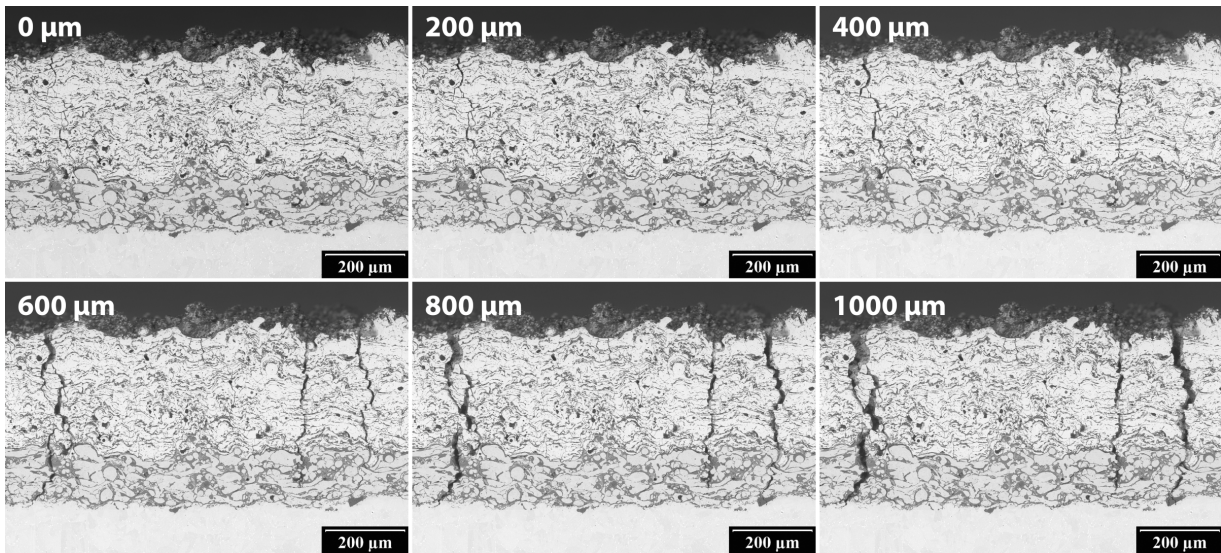


FIGURE 6. Evolution of cracking during in-situ test. Micrographs with deflection of 0, 200, 400, 600, 800, 1000 μm (from top-left to bottom-right) were selected.

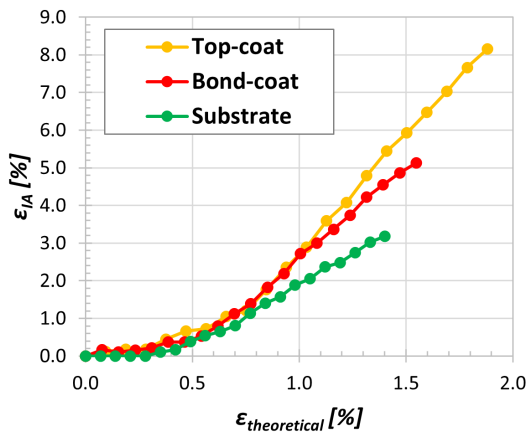


FIGURE 7. Plot of strain on the surface of each sub-layer evaluated by image analysis (IA) and from the sample deflection.

quire initial guess of maximum displacement value making batch processing significantly easier. Moreover, computing time does not increase significantly with increasing maximum displacement detected in the image, unlike in the original MATLAB-based code.

High resolution of the obtained strain maps showed not only the major cracking apparent already to the naked eye, but also minor changing of the coating microstructure as well as directly visualized the activation and de-activation of the crack networks.

First crack in the observed area initiated at the top-coat surface, and gradually propagated towards the substrate, later to be accompanied by a second crack initiated in the lateral distance of approx. $130 \mu\text{m}$. Second crack prevailed and its propagation led to the redistribution of the stresses within the coating and closing of the original crack. Nevertheless, both cracks propagated by through-splats cracking virtually regardless of the local coating microstructure, in

particular presence of secondary phase or splat boundaries. This in other words confirms again that the dissimilar interfaces were not the weak spots of the coating microstructure and that the coating possessed a rather high stiffness, eventually resulting in the limited coating strain tolerance.

Also after reaching the bond-coat, the cracks propagated perpendicularly to the bond-coat/top-coat interface. In this case, debonding of the splats was typical, especially when the oxides were present at the splat interface. However, intrasplat cracking and plastic necking of the metallic splats was also occasionally observed.

4. CONCLUSIONS

The carried out in-situ SEM 3PB experiment confirmed high cohesion of the deposited hybrid YSZ- Al_2O_3 coating as the induced cracks propagated dominantly by through-thickness splat cracking regardless of the local presence of the secondary miniature phase. Such behavior leads to the rather low strain tolerance of the coating, which led to relatively poor performance of this coating in the thermal cycling fatigue test when compared to conventional thermal barrier coatings which dissipate the straining energy more efficiently. This finding will be used in the deposition of the next set of hybrid TBCs with the aim of using deposition conditions favoring formation of less compact microstructure.

High-resolution strain mapping using pyramidal approach was confirmed to be a fast and strong tool for failure evolution assessment due to the direct visualization of the failure processes within the heterogenous coating microstructure. It is thus a welcome addition to the conventional fractography analysis, which is in the case of plasma sprayed coatings rather complicated as the as-deposited microstructure already contains numerous “defects” such as pores and pre-cracks.

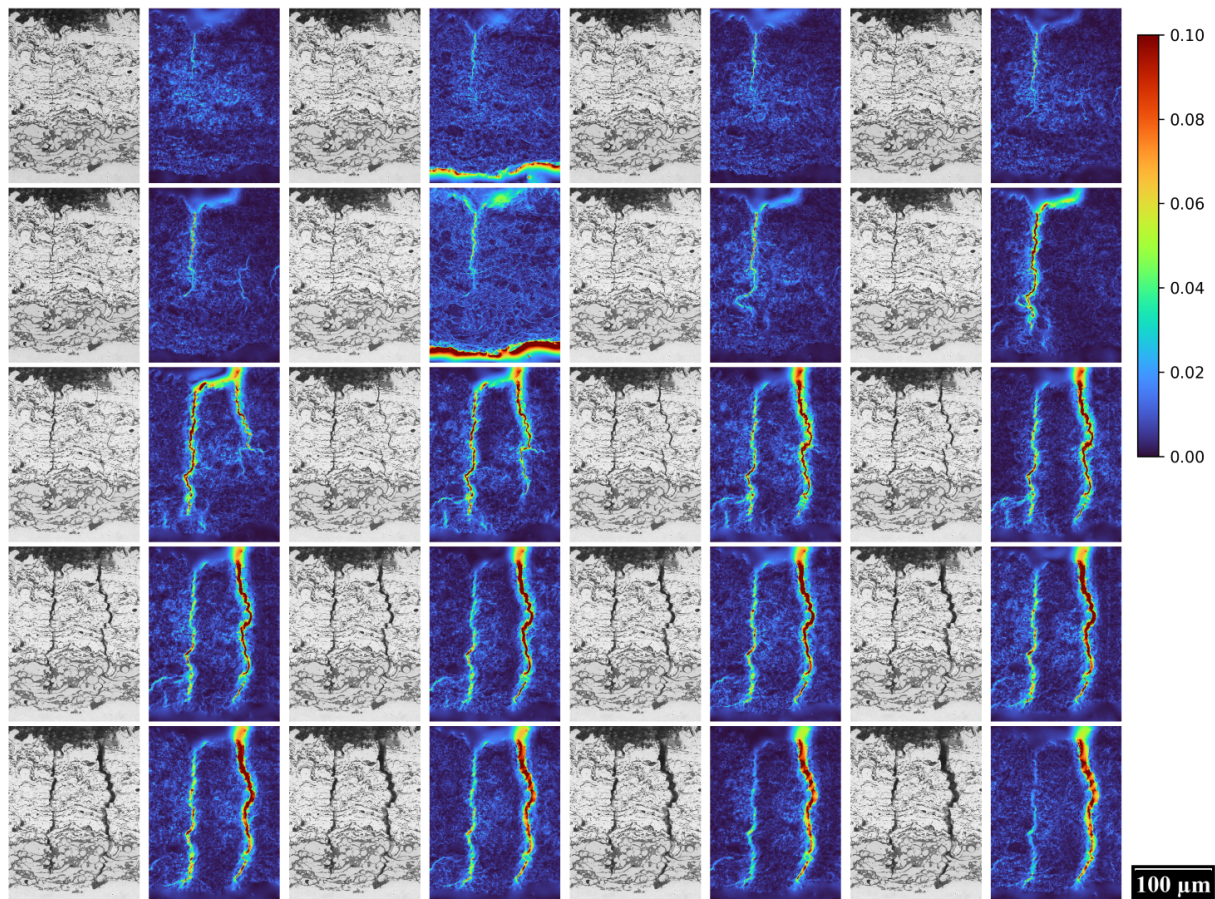


FIGURE 8. Equivalent strain maps showing propagation of the cracks above the central pin for each of the acquired SEM micrographs. Deflection step $50\ \mu\text{m}$ (from top-left to bottom-right). Strain maps were related to the previous stage (stepwise evaluation). Scale bar: $0.1 = 10\%$ equivalent deformation.

ACKNOWLEDGEMENTS

Financial support through project 22-21478S “High-enthalpy deposition of hybrid plasma spray coatings” funded by Czech Science Foundation is gratefully acknowledged.

REFERENCES

- [1] J. R. Davis. *Handbook of thermal spray technology*. ASM International, Materials Park, OH, USA, 2004.
- [2] P. Fauchais, G. Montavon, R. S. Lima, B. R. Marple. Engineering a new class of thermal spray nano-based microstructures from agglomerated nanostructured particles, suspensions and solutions: an invited review. *Journal of Physics D: Applied Physics* **44**(9):093001, 2011. <https://doi.org/10.1088/0022-3727/44/9/093001>
- [3] S. V. Joshi, G. Sivakumar, T. Raghuvver, R. O. Dusane. Hybrid plasma-sprayed thermal barrier coatings using powder and solution precursor feedstock. *Journal of Thermal Spray Technology* **23**(4):616–624, 2014. <https://doi.org/10.1007/s11666-014-0075-4>
- [4] S. V. Joshi, G. Sivakumar. Hybrid processing with powders and solutions: A novel approach to deposit composite coatings. *Journal of Thermal Spray Technology* **24**(7):1166–1186, 2015. <https://doi.org/10.1007/s11666-015-0262-y>
- [5] G. Bolelli, A. Candeli, L. Lusvarghi, et al. Tribology of NiCrAlY+Al₂O₃ composite coatings by plasma spraying with hybrid feeding of dry powder+suspension. *Wear* **344-345**:69–85, 2015. <https://doi.org/10.1016/j.wear.2015.10.014>
- [6] J. W. Murray, A. Leva, S. Joshi, T. Hussain. Microstructure and wear behaviour of powder and suspension hybrid Al₂O₃-YSZ coatings. *Ceramics International* **44**(7):8498–8504, 2018. <https://doi.org/10.1016/j.ceramint.2018.02.048>
- [7] R. Musalek, J. Dudik, T. Tesar, et al. Microstructure and thermal properties of the early-stage experimental thermal barrier coatings deposited by hybrid plasma spraying. *Journal of Thermal Spray Technology* **33**:732–745, 2024. <https://doi.org/10.1007/s11666-023-01708-w>
- [8] R. Musalek, T. Tesar, J. Minarik, et al. In-situ SEM observation of mechanical failure of hybrid plasma spray coatings. In *Thermal Spray 2024: Proceedings from the International Thermal Spray Conference*, pp. 266–277. 2024. <https://doi.org/10.31399/asm.cp.itsc2024p0266>
- [9] R. Musalek, M. Vilemova, J. Matejcek, et al. In-situ observation of ongoing microstructural changes in functionally graded thermal spray coating during mechanical loading. *Surface Modification Technologies XXVIII*:571–579, 2014.

- [10] A. Chabib, J.-F. Witz, P. Gosselet, V. Magnier. GPCPU_OpticalFlow: A GPU accelerated Python software for strain measurement. *SoftwareX* **26**:101688, 2024.
<https://doi.org/10.1016/j.softx.2024.101688>
- [11] M. G. D. Geers, R. De Borst, W. A. M. Brekelmans. Computing strain fields from discrete displacement fields in 2D-solids. *International Journal of Solids and Structures* **33**(29):4293–4307, 1996.
[https://doi.org/10.1016/0020-7683\(95\)00240-5](https://doi.org/10.1016/0020-7683(95)00240-5)
- [12] R. Musalek, T. Tesar, J. Dudik, et al. Cohesion of dissimilar splats in hybrid plasma sprayed coatings – A case study for Al₂O₃-TiO₂. *Journal of Thermal Spray Technology* **31**(6):1869–1888, 2022.
<https://doi.org/10.1007/s11666-022-01401-4>
- [13] A. Valarezo, G. Dwivedi, S. Sampath, et al. Elastic and anelastic behavior of TBCs sprayed at high-deposition rates. *Journal of Thermal Spray Technology* **24**(1-2):160–167, 2014.
<https://doi.org/10.1007/s11666-014-0154-6>